Unsupervised spectral clustering for segmentation of dynamic PET images

Hiba Zbib, Sandrine Mouysset, Simon Stute, Jean-Marc Girault, Jamal Charara, Sylvie Chalon, Laurent Galineau, Irene Buvat, Clovis Tauber

Unsupervised Spectral Clustering for Segmentation of Dynamic PET Images

Hiba Zbib, Sandrine Mouysset, Simon Stute, Jean-Marc Girault, *Member, IEEE*, Jamal Charara, Sylvie Chalon, Laurent Galineau, Irène Buvat, *Member, IEEE*, and Clovis Tauber, *Member, IEEE*

***Abstract*—Segmentation of dynamic PET images is needed to extract the time activity curves (TAC) of regions of interest (ROI). These TAC can be used in compartmental models for *in vivo* quantification of the radiotracer target. While unsupervised clustering methods have been proposed to segment PET sequences, they are often sensitive to initial conditions or favour convex shaped clusters. Kinetic spectral clustering (KSC) of dynamic PET images was recently proposed to handle arbitrary shaped clusters in the space in which they are identified. While improved results were obtained with KSC compared to three state of art methods, its use for clinical applications is still hindered by the manual setting of several parameters. In this paper, we develop an extension of KSC to automatically estimate the parameters involved in the method and to make it deterministic. First, a global search procedure is used to locate the optimal cluster centroids from the projected data. Then an unsupervised clustering criterion is tailored and used in a global optimization scheme to automatically estimate the scale parameter and the weighting factors involved in the proposed Automatic and Deterministic Kinetic Spectral Clustering (AD-KSC). We validate the method using GATE Monte Carlo simulations of dynamic numerical phantoms and present results on real dynamic images. The deterministic results obtained with AD-KSC agree well with those obtained with optimal manual parameterization of KSC, and improve the ROI identification compared to three other clustering methods. The proposed approach could have significant impact for quantification of dynamic PET images in molecular imaging studies.**

***Index Terms*—Clustering, segmentation of dynamic PET image, spectral clustering.**

I. Introduction

QUANTIFICATION of dynamic PET images brings *in vivo* information on the physiological and biochemical processes of organs. Time activity curves (TAC) are used in compartmental models in order to determine the kinetic parameters of organs under study. The TACs are calculated in regions which are often delineated manually by operators or from anatomical information. These manual delineations are time-consuming and subjective due to noise and poor spatial resolution of PET images. In addition, some radiotracers do not have identified anatomic regions of reference, e.g. radiotracers of neuroinflammation [1]. For such situations, it is not possible to use coregistered anatomic or atlas information. As a result, there is a growing interest in the development of clustering methods that aim at separating the PET image into functional regions. While supervised clustering methods have been proposed and successfully applied to neuroinflammation imaging using $[^{11}C]PK1195$[2], [3], they aim at describing the TAC of each voxel as a combination of several sources, and often rely on kinetic classes that have to be previously defined. Unsupervised methods can be used for the definition of such classes, or for the segmentation of dynamic PET images into functional regions with no a priori on the scanner or radiotracer used. In this work, we focus on unsupervised methods to identify clusters of voxels with homogeneous kinetic behaviors. Such methods can be divided into three categories:

- Methods based on the temporal behavior of voxels;
- Methods analyzing the spatial and temporal information associated with each voxel;
- Methods that cluster the dynamic PET data directly in the sinogram domain.

Among the methods using the temporal information of the PET sequence, Wong *et al.*[4] segmented the dynamic PET image using a K-means algorithm. Kimura *et al.*[5] clustered the voxels based on the first two principal components of the TACs of voxels to segment the image and calculate the kinetic parameters. Brankov *et al.*[6] used a similarity measure that depends on the shape of the TAC rather than its amplitude and modeled the intra-cluster variation by a truncated exponential probability density distribution, then applied an expectation-maximization approach to identify the clusters. Margadan-Mendez *et al.* [7] extracted the cardiac tissue components by an iterative independent component analysis. Saad *et al.* [8] simultaneously estimated physiological parameters and the TACs of clusters by least-square optimization using a method that requires the input function. Guo *et al.* [9] presented a method for parametric PET imaging that combines a preclustering process using a histogram-based thresholding with a hierarchical cluster analysis. Zheng *et al.* [10] proposed a three-stage clustering algorithm: first they removed the background by K-means clustering, then they modeled the TAC

The research leading to these results has received funding from the European Union's Seventh Framework Programme (FP7/2007-2013) under grant agreement no HEALTH-F2-2011-278850(INMiND).

H. Zbib is with UMRS INSERM U930 - Université de Tours, 37032 Tours, France, and also with Université Libanaise, Al Hadath, Lebanon.

S. Mouysset is with CNRS UMR 5055 - Université de Toulouse, 37032 Tours, Toulouse.

S. Stute and Iréne Buvat are with CEA, Service Hospitalier Fréedéric Joliot, 91401 Orsay, France.

J.-M. Girault, S. Chalon, L. Galineau, and C. Tauber are with UMRS INSERM U930 - Université de Tours, 37032 Tours, France (e-mail: clovis.tauber@univ-tours.fr).

J. Charara is with the Université Libanaise, Al Hadath, Lebanon.

Color versions of one or more of the figures in this paper are available online at http://ieeexplore.ieee.org.

Digital Object Identifier 10.1109/TNS.2015.2399973

using polynomial regression mixture models for detecting the heart structure, finally a hierarchical clustering was applied for ROI refinements. The main limitations of these methods are that they either depend on initial conditions or on an *a priori* kinetic model and that they are not appropriate for the segmentation of clusters with an arbitrary shape in the feature space. Methods in the second category use the spatial location and the TAC kinetic features as input for the segmentation algorithm: Parker *et al.* [11] proposed a graph-based method for the minimization of Mumford-Shah energy in order to estimate the input function directly from the carotid artery. After pre processing the data with principal component analysis, their method used the Mahalanobis distance as a similarity measure. Kim *et al.* [12] integrated the spatial and temporal information in a hybrid method that uses both cluster analysis and region growing. Chen *et al.* [13] worked on Markov random fields for simultaneous estimation of parameters and segmentation of the image by expectation-maximization. The integration of spatial information increases the robustness to noise, however it can also prevent from correct clustering of distant regions with homogeneous kinetic profiles and an additional parameter has to be set to control the trade-off between spatial and kinetic proximity. To circumvent this problem, Maroy *et al.* [14] estimated the pharmacokinetics based on voxels far from organ borders and segmented the rodent whole-body PET images using a local-mean analysis method followed by a hierarchical linkage algorithm to merge regions with similar TAC. The third category of segmentation of dynamic PET images includes methods that cluster the dynamic PET images directly in the sinogram domain. Krestyannikov *et al.* [15] separated the dynamic tomographic data directly in the projection space using the least-square method. Kamasak *et al.* [16], [17] clustered dynamic PET images in the sinogram domain by assuming that the sinogram had either a Poisson or a Gaussian distribution. They also proposed a parametric iterative coordinate descent (PICD) algorithm for direct nonlinear estimation of kinetic parameters at each voxel from dynamic PET sinogram data [18].

Recently we have proposed an approach based on spectral clustering for segmentation of dynamic PET images called Kinetic Spectral Clustering (KSC) that has the advantage of handling arbitrary shaped clusters in the feature space [19]. This method achieved better segmentation accuracy compared to several conventional clustering algorithms. In this paper we improve the previously proposed method by deriving an automatic and deterministic spectral clustering algorithm (AD-KSC) for segmentation of dynamic PET images. First, we replace the last step of the method by a modified version of the K-means algorithm that operates global optimization for identifying cluster centroids. Second, we combine an original unsupervised criterion and a probabilistic metaheuristic to automatically estimate both the scale parameter of the method and the weight to be associated with each frame of the dynamic PET sequence. To validate our approach, GATE Monte Carlo simulations of the Zubal head phantom and of a sphere phantom were performed. The AD-KSC was evaluated on these simulated phantoms and was compared to 3 unsupervised methods from the literature. Results on real microPET images are also presented.

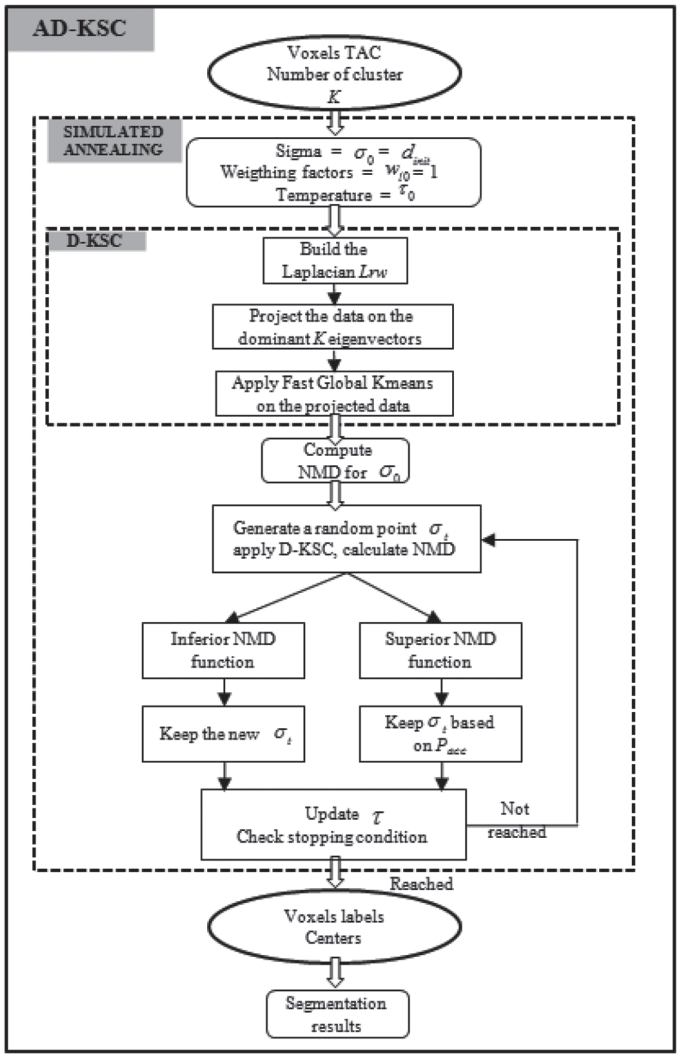

Fig. 1. Flowchart of the proposed AD-KSC algorithm.

II. Proposed Method

A. Principle of the AD-KSC Method

The AD-KSC method includes 5 steps as described below:

1. The air surrounding the phantom or the subject is removed using histogram-based thresholding.
2. The affinity between all pairs of TACs is calculated and the data are projected on a new feature space.
3. A deterministic algorithm is used to cluster the projected data.
4. The parameters of AD-KSC are estimated using a global iterative optimization process of a proposed unsupervised criterion.
5. The dynamic PET sequence is segmented using the optimal parameters selected in step 4.

A global flowchart of the AD-KSC approach is presented in Fig. 1.

TABLE I
MAIN ACRONYMS OF AD-KSC ALGORITHM IN ORDER OF APPEARANCE

PET	Positron emission tomography
TAC	Time activity curve
KSC	Kinetic Spectral Clustering
D-KSC	Deterministic Spectral Clustering
AD-KSC	Automatic and Deterministic Spectral Clustering
K	Number of functional regions
T	Number of frames of the PET image series
N	Number of voxels to be clustered
X_i	TAC of voxel i
$S(X_i, X_j)$	Similarity between TAC of voxels i and j
σ	Scale parameter of the spectral clustering kernel
w_l	The weighting factor of frame l
W	Vector of all weighting factor w_l
$d(X_i, X_j)$	Weighted euclidian distance between TACs of voxels i and j.
C_l	Mean TAC of voxels in cluster l (cluster centroid in feature space)
NMD	Normalized Minimal distance.
δ_{min}	Minimal inter cluster distance.
Δ_{max}	Maximal intra cluster distance.
$dl_{95^{th}}$	95 percentile of the intra cluster distance in the cluster l.
SA	Simulated Annealing
P_{acc}	Probability of acceptance of a worse point used by SA
Δ	Difference in the objective function NMD
d_{min}	Minimal distance between all pairs of X_i
$d_{90^{th}}$	90^{th} percentile of the distance between all pairs of X_i
d_{init}	Average distance between each X_i and its closest neighbor

B. Notations

Let us K denote the number of functional regions, T the number of frames contained in the PET sequence, N the number of voxels to be clustered, $X_i \in \mathbb{R}^T$ the measured time activity curve (TAC) in voxel $i \in [1 \dots N]$ and W the weights vector. Table I lists the main notations and acronyms in their order of appearance in the paper.

C. Prior Histogram-Based Thresholding

The air around the object contains reconstruction artefacts and noise. We remove this region by thresholding the summed sequence. All the frames of the PET sequence are summed, and the logarithms of the values in the sum image are sorted in increasing order. The threshold value is extracted as proposed in [14], and a mask of the studied animal or subject is obtained. "Holes" or strong discontinuities are removed using standard morphological closing operators.

D. TAC Affinity and Feature Space Projection

We previously reported the feasibility of segmentation of dynamic PET images using kinetic spectral clustering [19]. This section describes the calculation of affinity between TACs and the feature space definition that are involved in AD-KSC.

Mapping into High Dimensional Space: spectral clustering can be viewed as partitioning an undirected graph into a set of K discrete clusters. In this work the number of clusters K is supposedly known *a priori*. Each node in the graph corresponds to a temporal behavior or TAC of a voxel and the edge between two nodes has an associated numerical value that corresponds to the similarity between the TAC of the voxels it connects. The segmentation of dynamic PET images by kinetic spectral clustering starts with the calculation of the similarity between all pairs of TACs using a Gaussian kernel function to project the data into a high dimensional space. The entries of the similarity matrix are calculated as [20]:

$$S(X_i, X_j) = \exp \frac{-d(X_i, X_j)^2}{2\sigma^2}, \tag{1}$$

where $S(X_i, X_j)$ is the similarity between the TACs of voxels i and j, σ is a scale parameter that adjusts the distance of patterns mapped into the feature space, and $d(X_i, X_j)$ is a weighted Euclidean distance that we defined as [19]:

$$d(X_i, X_j) = (\sum_{l=1}^{T} w_l (X_i(l) - X_j(l))^2)^{1/2} \tag{2}$$

where w_l is the weighting factor of frame l. The noise level in dynamic PET images can differ significantly between frames. Therefore in KSC, we weighted the frames by the inverse of their noise variance in the calculation of the distance between TACs to increase the confidence in frames having less noise [19], [21]. In AD-KSC we use a different strategy as the weights are automatically estimated, as described in Section II-G.

Projection on a low dimensional space: A Laplacian random walk matrix denoted by L_{rw} is derived from the similarity measure [22]. Spectral clustering using L_{rw} can be interpreted as trying to identify a partition of the graph such that the random walk stays long within the same cluster and seldom jumps between clusters. The K dominant eigenvectors of L_{rw} are used to project the data on a reduced space where the natural clusters in the data become more linearly separable.

E. Deterministic Search for Centroids in Feature Space

The K dominant eigenvectors of the Laplacian matrix span a lower dimensional space wherein data are better separated and often clustered by the K-means algorithm, as proposed in KSC [19]. The K-means is a stochastic procedure that starts from a random initialization and locates the centers that minimize the clustering error criterion. While being cost-effective, the K-means does not necessarily reach the global minimum of the clustering criterion, as it depends on the initial conditions and several runs from different starting centers can be necessary to obtain the best result. To avoid dependency on initial conditions, we define a Deterministic Spectral Clustering (D-KSC) in which we replace the last step of KSC for Global K-means (GKM) [23], a deterministic version of K-means that operates global optimization to identify the cluster centroids.

The GKM is an incremental approach that dynamically adds one cluster center at a time. Unlike the K-means algorithm, the GKM algorithm always starts from the same centers, which are iteratively selected from the data themselves, in order to obtain deterministic clustering of the data. It selects the centers that minimize a clustering error criterion defined by [23]:

$$E(C_1, ., C_K) = \sum_{i=1}^{N} \sum_{l=1}^{K} A(X_i \in l) \| X_i - C_l \|^2) \tag{3}$$

where $C_l \in \mathbb{R}^T$ is the mean TAC of voxels belonging to cluster l, $\| X_i - C_l \|^2$ is the squared Euclidean distance between X_i and

C_l, and A is a Boolean function such that $A(Y) = 1$ if Y is true and 0 otherwise.

To reduce the time needed for GKM convergence we used the fast global K-means with kd-tree structure and we set the number of buckets to $10K$[23]. In the remaining of this paper GKM represents the fast global K-means with kd-tree.

F. Unsupervised Normalized Minimal Distance Criterion

The unsupervised estimation of optimal input parameters relies on the definition of an appropriate quality criterion. Several approaches have been proposed in the literature: Rezaee *et al.* [24] proposed a validity index that assesses the intra cluster variance and the separation between clusters. Zahid *et al.* [25] proposed a cluster-validity criterion that considers the geometrical properties and the degree of fuzzy membership. Halkidi *et al.* [26] proposed a criterion composed of two measures assessing the separation between clusters and the compactness of each cluster. Davies and Bouldin [27] proposed a ratio between the sum of within cluster scatter and the sum of between clusters scatter. Dunn [28] proposed a widely used cluster validity index that corresponds to the ratio between the minimal inter-cluster distance to the maximal intra-cluster distance. The inter-cluster distance is often chosen either as the minimal distance between elements assigned to different clusters or as the minimal distance between the centroids of the clusters. The intra-cluster distance is generally measured either as the maximal distance between any pair of elements in the cluster, or as the average distance between elements of the clusters. While the Dunn index (DI) has been used in various applications, it is very sensitive to noise and not adapted to PET images where the voxels TACs from the same functional region are very noisy due to the physical properties of this imaging modality. A robust criterion of cluster quality is needed to select the segmentation results with compact and well separated clusters. We propose an unsupervised criterion that extends the Dunn index by making it more robust in the calculation of the diameter of the clusters. We call the proposed criterion Normalized Minimal Distance (NMD) and define it as:

$$NMD = \frac{\delta_{min}}{\Delta_{max}^{95}}, \tag{4}$$

where δ_{min} is the minimal inter-cluster distance that decreases when voxels presenting similar time courses are assigned to different clusters, and is defined by:

$$\delta_{min} = \min_{1 \leq o < p \leq K} \|C_o - C_p\|, \tag{5}$$

where C_o and C_p are the centers of clusters o and p respectively and $\|C_o - C_p\|$ is the Euclidean distance between these two centers. Δ_{max}^{95} is a robust maximal intra-cluster distance, which increases when voxels with distinct kinetics are grouped into the same cluster. Δ_{max}^{95} is defined as:

$$\Delta_{max}^{95} = \max_{1 \leq l \leq K} \left(\frac{\sum_{i,j \in l} \|X_i - X_j\| A(\|X_i - X_j\| \geq dl_{95^{th}})}{N_l \times 0.05} \right), \tag{6}$$

where dl_{95}th is the 95 percentile of intra-cluster distances of cluster l and N_l is the number of voxels belonging to l. Δ_{max}^{95} is based on the 5% largest intra cluster distances to obtain a robust estimate of the cluster diameter. Large values tend to suggest that two clusters have erroneously be merged. Δ_{max}^{95} is more robust than a cluster distance based on far away data points and is not penalized by small distances between similar profiles. The proposed NMD criterion decreases when a merging or splitting of clusters occurs.

G. Global Optimization of NMD

In AD-KSC, two parameters can impact the accuracy of clustering: the scale parameter σ and the vector of weights factors W. In previous work [19], the weighting factors of the different frames were the inverse of a noise variance estimate based on frame duration, time since injection and number of counts. While this weighting scheme proved to be appropriate, it ignores changes in contrast between ROIs across frames, making it difficult to segment ROIs that are better distinguishable in time frames highly affected by noise. Estimating the correct noise variance has been tackled with several approaches in the literature [29], [30], [31], [32], [33]. In AD-KSC, rather than calculating the weights from data statistics or manually setting the scale parameter, we propose to automatically set both the weighting factor of each frame and the scale parameter σ by optimizing the NMD criterion. A Simulated Annealing (SA) [34] approach is used to locate a good estimate of the criterion global optimum. This algorithm consists in first melting the system being optimized at a high effective temperature, then lowering the temperature by slow stages until the system freezes and no further changes occur. At each step the parameter values are randomly perturbed, and the cost function is calculated using $-NMD$. Downhill steps are always accepted, whilst uphill steps are accepted to step out of a local minimum under a probability acceptance function. The probability of acceptance depends on the NMD objective function value and on the current temperature τ and is defined as:

$$P_{acc} = \begin{cases} 1 & if \Delta \leq 0 \\ (1 + e^{\Delta / \tau k_B})^{-1} & otherwise, \end{cases} \tag{7}$$

where $\Delta = NMD(u+1) - NMD(u)$, u is the number of iteration, τ is the current temperature, and k_B is the Boltzmann constant.

Bound constraints and initialization of AD-KSC parameters: The Gaussian parameter σ adjusts the distance of patterns mapped into the feature space; it controls the size of the neighborhood between points. Proper selection of this parameter therefore directly affects clustering accuracy. When σ has a magnitude equivalent to the maximal distance between points, most patterns in the feature space are close to each other and it is often difficult to separate them. When its magnitude is equivalent to the minimal distance, all points are far from each other and these patterns tend to fall into the orthogonal subspace where hyperplanes can arbitrarily divide some patterns. Therefore, we propose to set the bounds for the setting of this scale parameter to the interval ranging from the minimal

distance between all pairs of TACs to the 90^{th} percentile of the distances between all pairs of TACs. We initialize the scale parameter to the average of the distance between each point and its closest neighbor (which we denote d_{init}) to ensure that the SA algorithm starts from a suitable estimation of the scale parameter. d_{init} is defined as:

$$d_{init} = \frac{1}{N}\sum_{i=1}^{N} \min_{\substack{1\leq j\leq N \\ j\neq i}} \|X_i - X_j\|. \quad (8)$$

The initial temperature was set to $\tau_0 = 100$. The maximal number of SA iterations was set to 50 iterations. The bounds of the weighting factors were set to $\forall l, w_l \in [0,1]$; while the initial values for all frames were set to $w_{l0} = 1$.

III. Assessment Of the AD-KSC Method

A. Simulation of Realistic PET Images

TAC associated with brain regions were derived from the three-compartment model proposed by Kamasak *et al.* [18] and Maroy *et al.* [14]. A homogeneous vascular fraction was assumed in each region. The input function was denoted C_{plas} and was given by:

$$C_{plas}(t) = B_0[(B_1 t - B_2 - B_3)e^{-\gamma_1 t}) + B_2 e^{-\gamma_2 t} + B_3 e^{-\gamma_3 t}]. \quad (9)$$

The kinetic of the tissue compartment i, denoted $C_{tissue(i)}$, was computed as:

$$C_{tissue(i)} = (\sum_{y=1}^{3}[a_{i,y}e^{-t/b_{i,y}}] * C_{plas}) \quad (10)$$

where $*$ denotes the convolution operator. Parameters B_0, B_1, B_2, B_3, λ_1, λ_2, λ_3, $a_{i,y}$ and $b_{i,y}$ were randomly set using the constraints proposed by Maroy *et al.* [14]. A constant vascular fraction of 5% was considered in each ROI. Sample TACs used for simulations are shown in Fig. 2. GATE Monte Carlo simulations of Philips Gemini GXL PET 4D acquisitions were performed [35], [36]. Two phantoms were used for the simulations: a phantom consisting of six spheres with different diameters within a cylinder (simulation 1), and the labeled MR image of the Zubal head phantom (simulations 2 and 3) [37]. The regions of the Zubal head phantom considered for the simulation were: the frontal, occipital, parietal, cerebellum and thalamus regions and the remaining parts of the head (called background) plus a seventh region with no activity corresponding to the air around the head. These regions were the ground truth for the evaluation of the results. We generated the sets of TACs for each region of the phantoms using (10) and simulated three dynamic sequences called simulations 1, 2 and 3 hereafter. Simulations 1 and 2 consisted of 5×30 s followed by 15×60 s dynamic frames, while simulation 3 consisted of 6×30 s, 4×1min, 4×2min, 5×5min followed by 1×10min. Radiation decay was modeled. The total number of coincidences for each time frame varied between 5 and 70 millions. In order to assess the quality of segmentation at different noise levels we used different sets of simulation and reconstruction parameters in the 3 simulations, which are summarized in Table II. The reconstruction of dynamic PET images was performed with a fully 3D ANW-OSEM iterative method, followed by a 5 mm FWHM Gaussian smoothing. The dynamic PET images were divided by their average intensity value so as to work with scale parameters of the same order of magnitude between the different simulations.

TABLE II
Parameters Used for the Simulation of the 3 PET Sequences

	Sim.1	Sim.2	Sim.3
Phantom	Sphere	Zubal	Zubal
Simulated attenuation	yes	no	yes
Attenuation correction	yes	no	yes
Normalization	yes	no	yes
Iteration numbers	2 iteration	5 iterations	10 iterations
Subset numbers	16 subsets	8 subsets	16 subsets
Noise level	$++$	$+$	$+++$
Average prompts (million)	36.6	47.2	34.2
Average randoms (%)	18.9	14.1	33.1
Average scatters (%)	29.9	4.8	26.6

B. Quantitative Assessment of the Results

In addition to the unsupervised NMD criterion, the quality of segmentation results was assessed using two supervised criteria.

Pratt's Figure of Merit (PFOM): Pratt's figure of merit measures the precision of edge locations in segmented images, compared to their ground truth locations. The PFOM was calculated as follows:

$$PFOM = \frac{1}{max(N_I, N_D)}\sum_{i=1}^{N_D}\frac{1}{1+\alpha d_i^2} \quad (11)$$

where N_I and N_D respectively are the number of ideal and detected edge voxels, d_i denotes the distance from the ith-detected edge voxel to the nearest ideal edge voxel and α is a scaling constant set to 1/9 as in Pratt's work [38].

Adjusted Rand Index (ARI): The Adjusted Rand Index [39] assesses the consistency between ground truth regions and estimated regions. This criterion accounts for the number of pair of voxels grouped into the same or different clusters.

These two supervised criteria have values between 0 and 1. When the segmented results perfectly agree with the ground truth, these criteria are equal to 1.

C. Comparison of AD-KSC with Other Methods

- K-means (KM): Wong *et al.* proposed to cluster dynamic PET data with a K-means approach [4]. The K-means is an effective method with low computational cost. After a random initialization of the centers, it iteratively determines the partition of data that minimizes their distances to the clusters centroids. In all experiments, we selected the results that maximized the NMD criterion over 100 runs of KM.
- Expectation-maximization (EM): Ashburner *et al.* proposed an EM approach for the characterization of dynamic PET data. Expectation-Maximization is a model-based approach in which clusters are described as a parametric

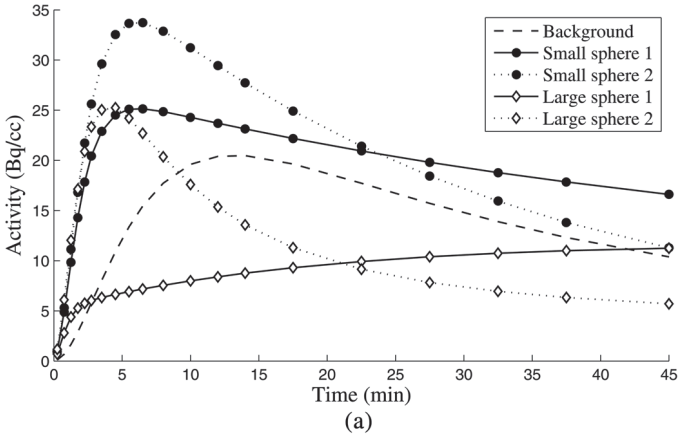

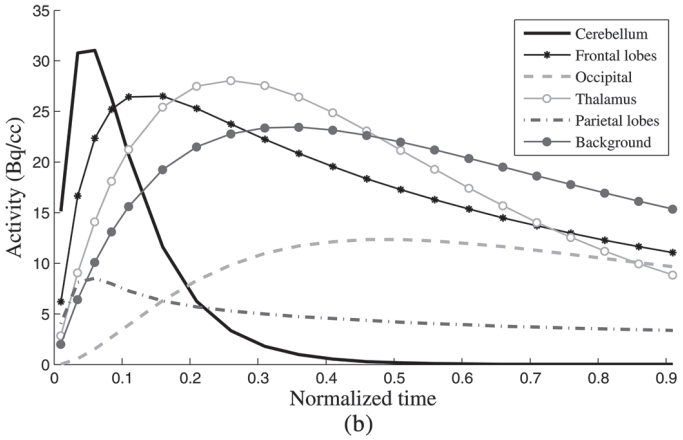

Fig. 2. TACs used to simulate two of the dynamic PET image series. (a) Sphere phantom (b) Zubal head phantom (simulation 2).

Gaussian distribution. The method consists in finding the maximum likelihood estimates of parameters [40].

- Hierarchical method (HC): Guo *et al.* [9] proposed a hierarchical method based on average linkage for dynamic PET data clustering. The agglomerative hierarchical clustering consists in merging clusters iteratively. We used the average linkage cluster method to calculate the distance between clusters. To avoid solutions in which a cluster would include a single data point, K + 10 clusters were calculated (K being the number of clusters in the ground truth), and the clusters were manually merged with other clusters so as to maximize the NMD criterion.
- Kinetic Spectral Clustering (KSC): The spectral clustering algorithm [19] with K-means in the last step of the method and manual setting of the scale parameter σ was used for comparison with D-KSC and AD-KSC, to assess both the deterministic properties and the efficiency of the automatic parameter selection.

D. Real Data Set

The AD-KSC was applied to $[^{18}F]LBT999$ PET images of the dopamine transporter [41] of rats acquired with a GE Vista microPET/CT. Using these images, AD-KSC was compared to the KM, EM and HC algorithms. Rats were scanned during 4×10 s, 4×20 s, 4×60 s, 8×180 s, 5×360 s, 1×340 s and 1×260 s and the corresponding PET images were reconstructed using a 2D OSEM iterative method. Images were registered into Paxinos coordinates using Pmod 3.3 and the Schiffer Atlas [42] was used to assess the segmentation result as a substitute to ground truth, given that a striatal uptake was expected.

E. Comparison of NMD with other Unsupervised Criteria

We compared the proposed NMD criterion with the Dunn index (DI). The Dunn index is defined as [28]:

$$DI = \min_{1\leq i\leq K}\left(\min_{1\leq j\leq K}\left(\frac{\min\limits_{x_o\in A, x_p\in B}(d(x_o,x_p))}{\max\limits_{1\leq k\leq K}\max\limits_{x_n,x_m\in C}(d(x_n,x_m))}\right)\right), \quad (12)$$

The numerator measures the separation between clusters A and B; the denominator corresponds to the diameter of cluster C.

IV. Results

A. Comparison of AD-KSC with Other Approaches

Fig. 3 displays representative results of the clustering obtained for simulation 1. On this representative slice, the number N of voxels considered for clustering was 3672. EM, KM and HC algorithms (Fig. 3(c)–(e)) correctly detected two big spheres, merged the small spheres and separated the background into two parts. AD-KSC correctly identified all regions (Fig. 3(f)). Two opposite trends were observed regarding the small spheres: EM, KM and HC methods tended to overestimate their size while AD-KSC underestimated them. AD-KSC was the only method able to distinguish the two smallest spheres.

First row in Fig. 4 displays representative results of the clustering obtained for simulation 2, where the level of noise was the lowest among all simulations. On this representative slice, the number N of voxels considered for clustering was 4390. The EM algorithm (Fig. 4(d)) merged the frontal lobe with the thalamus, and the parietal lobe was associated with the background, which was separated into several parts. The HC algorithm (Fig. 4(e)) merged the parietal lobe with the background and correctly detected the remaining regions. KM (Fig. 4(c)) produced a noisy background while it detected the regions more accurately than EM and HC. However compared to the ground truth, the sizes of the parietal and occipital lobes were bigger, which was not the case with AD-KSC (Fig. 4(f)) where all regions were correctly and more precisely detected.

Figs. 4(g)–(l) display representative clustering results obtained for simulation 3. Compared to simulation 2, the attenuation and the normalization were included in this simulation and the number of iterations was higher than for other simulations, which resulted in a higher level of noise. KM and EM algorithms (Fig. 4(i)–(j)) did not detect the thalamus and several ROI were merged with the background. The HC algorithm merged the thalamus with the background and the frontal lobe, and also merged the occipital and the parietal lobe (Fig. 4(k)). With AD-KSC (Fig. 4(l)), the background was less associated with other regions. The parietal, occipital and frontal lobe were correctly detected, but the thalamus was not detected. In this simulation, the four methods misclassified some

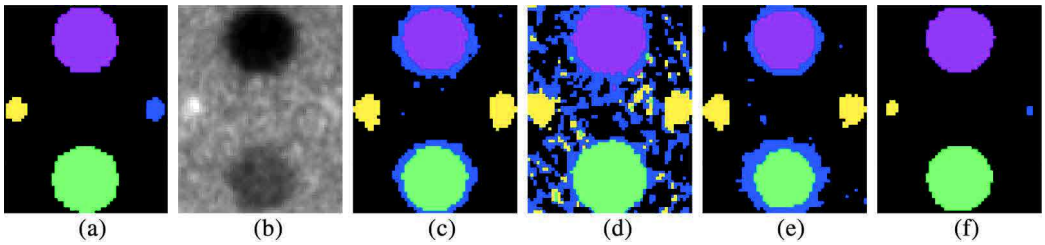

Fig. 3. Axial views of the results obtained with simulation 1: (a) ground truth, (b) one frame from the simulated image, (c) KM, (d) EM, (e) HC, (f) AD-KSC.

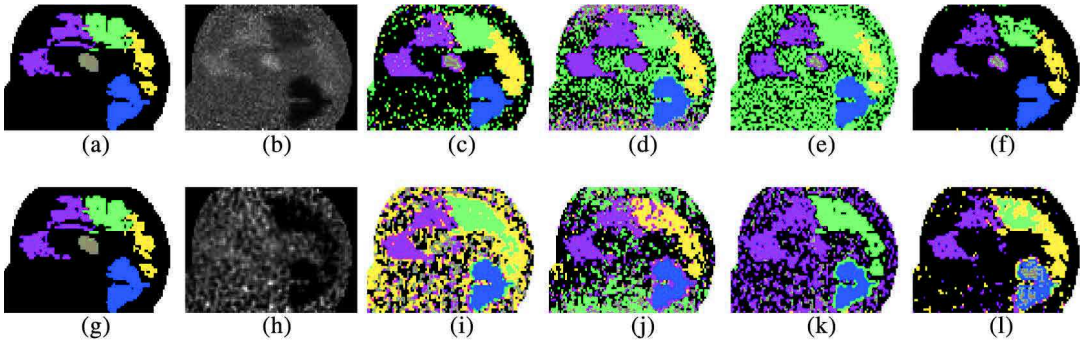

Fig. 4. Sagittal views of the results obtained with simulations 2 and 3. First row: sagittal view of the results obtained for simulation 2: (a) ground truth, (b) one frame from the simulated image, (c) KM, (d) EM, (e) HC, (f) AD-KSC. Second row: sagittal view of the results obtained for simulation 3: (g) ground truth, (h) one frame from the simulated image, (i) KM, (j) EM, (k) HC, (l) AD-KSC.

TABLE III
VERAGE AND STANDARD DEVIATION OF THE QUANTITATIVE CRITERIA

Phantoms	Criteria	KM	EM	HC	AD-KSC
Simulation 1 Sphere (2it,16sb)	ARI	0.62 ± 0.32	0.20 ± 0.13	0.70 ± 0.18	**0.79 ± 0.20**†
	PFOM	0.84 ± 0.20	0.49 ± 0.08	0.82 ± 0.20	**0.95 ± 0.04**†
	NMD	0.57 ± 0.20	0.03 ± 0.02	0.66 ± 0.45	**1.23 ± 0.54**†
Simulation 2 Zubal (5it,8sb)	ARI	0.73 ±0.13	0.58 ± 0.23	0.71 ± 0.17	**0.86 ± 0.06**†
	PFOM	0.80 ± 0.11	0.76 ± 0.12	0.80 ± 0.13	**0.93 ± 0.05**†
	NMD	0.18 ± 0.09	0.09 ± 0.09	0.17 ± 0.08	**0.30 ± 0.10**†
Simulation 3 Zubal (10it,16sb)	ARI	0.54 ±0.23	0.52 ± 0.22	0.66 ± 0.18	**0.75 ± 0.16**
	PFOM	0.73 ± 0.08	0.72 ± 0.11	0.78 ± 0.12	**0.84 ± 0.09**
	NMD	0.15 ± 0.07	0.08 ± 0.07	0.12 ± 0.07	**0.19 ± 0.09**†

functional regions and especially the thalamus, parietal and occipital lobes. The voxels of the thalamus were very affected by both the noise and the partial volume effect. In AD-KSC the misclassification of the thalamus led to the splitting of another region, which corresponded to the cerebellum.

Table III presents the averages and the standard deviations of the quantitative criteria calculated for 8 2D + t slices from simulation 1, and 20 2D + t slices from simulations 2 and 3, using KM, EM, HC and AD-KSC. In every row of the table, the maximum average value is indicated in bold. The † symbol indicates a significant difference ($p < 0.05$) between the AD-KSC average score and the second highest average score, using a non-parametric Wilcoxon paired test. ARI, PFOM, and the absolute value of NMD were the smallest for the EM algorithm, while they were the highest for AD-KSC in the 3 simulations. The scores obtained with AD-KSC indicate an increase in the identification accuracy of functional regions compared to other methods.

B. Deterministic Property of D-KSC

We assessed the variability of the segmentation of KSC and D-KSC over 50 replicated runs on the same slice for given scale and weighting factors. Three quantitative criteria ARI, PFOM, NMD were calculated for these two methods over the 50 replicated runs and are shown in Fig. 5. The results of KSC varied significantly from one run to another. With KSC, the average NMD score for these replicated runs was 0.13 ± 0.11, the average ARI score was 0.75 ± 0.06 and the average PFOM score was 0.87 ± 0.10. The results of D-KSC were constant for all 50 runs, NMD score was 0.27 ± 0.00, ARI score was 0.82 ± 0.00 and PFOM was 0.97 ± 0.00 in average. D-KSC yielded the maximum score of ARI, PFOM, and NMD criteria that could be obtained with KSC over the 50 runs.

C. Variation of NMD versus ARI and PFOM Criteria

Variations of the KSC scores shown in Fig. 6 show that NMD varied consistently with the supervised ARI and PFOM criteria.

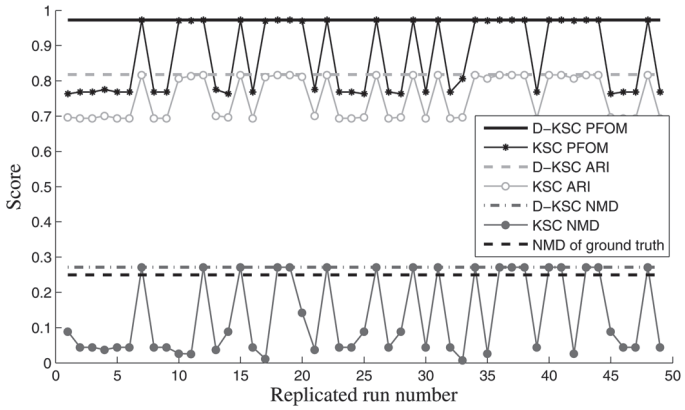

Fig. 5. Figures of merit of replicated runs of KSC and D-KSC on a 2D + t slice of simulation 1.

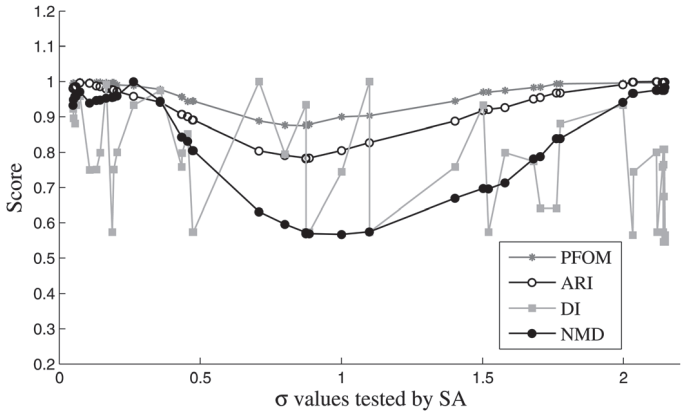

Fig. 6. Figures of merit obtained for different values of σ estimated using simulated annealing during a run of AD-KSC on simulation 3 (Maximum value of each figure of merit was set to 1).

For most measured values, when ARI and PFOM increased, the value of NMD increased also and vice versa. The correlation coefficients with the value of the unsupervised NMD criterion were equal to 0.75 for PFOM and 0.77 for ARI.

D. Comparison Between Unsupervised (NMD, DI) and Supervised (ARI, PFOM) Criteria

Fig. 6 displays plots of the PFOM, ARI, DI, and NMD scores obtained for various values of σ that were tested by SA during the parameter optimization. DI exhibits many fluctuations, while the variations of NMD were consistent with the variations of ARI and PFOM. The correlation coefficients between the supervised and unsupervised criteria were 0.94 between ARI and NMD, and 0.91 between PFOM and NMD. They were -0.08 between PFOM and DI, and -0.10 between ARI and DI.

E. Parameters Estimation of AD-KSC

AD-KSC is the automatic and deterministic extension of KSC. Therefore, it aims at producing results that are as close as possible to the best KSC results that can be obtained with manual setting of the parameters. We thus determined the maximal ARI and PFOM scores that could be obtained by manually changing the parameters of KSC. Then for 8 slices from simulation 1, and for 20 slices from simulations 2 and 3, we calculated the ARI and PFOM scores obtained with AD-KSC and expressed them as a percentage of the maximal scores that could be obtained with KSC. Table IV displays the resulting ratios of maximal achievable scores. The NMD criterion perforrmed well at selecting the parameters that gave accurate segmentation with a percentage of maximal achievable score between 93% and 98%.

TABLE IV
AD-KSC SCORES EXPRESSED AS A PERCENTAGE OF MAXIMAL KSC SCORES OBTAINED FROM MANUAL SETTING OF THE PARAMETERS

	Sim.1	Sim.2	Sim. 3
ARI AD-KSC	93 %	98 %	93 %
PFOM AD-KSC	98 %	97 %	93 %

F. Simulated Annealing Reproducibility

Table V presents the averages and the standard deviations calculated for the quantitative ARI, PFOM, and NMD criteria for 20 runs of the AD-KSC algorithm over six different dynamic images from simulations 1, 2, and 3. These criteria were found very stable along the 20 runs. The parameters (sigma and weights vector) selected by AD-KSC presented small variations but they did not significantly modify the segmentation quality of the PET images.

G. Real Data Experiments

Fig. 7 shows the results obtained with KM, EM, HC and AD-KSC on a real $[^{18}F]LBT999$ PET image. In the presented slice, the number N of voxels considered for clustering was 7324, and the number of clusters K was set to 3. All methods correctly detected the functional regions and the results for all methods were close. However the brain structures were slightly better delineated with AD-KSC than with the other methods when compared to the atlas edges. For the four algorithms part of the background region was merged with the whole brain, but this was less pronounced for AD-KSC. The mean TACs of regions segmented by AD-KSC are plotted in Fig. 8. These TACs correspond with the expected TACs in the striatum, whole brain and background.

We compared the results of AD-KSC obtained with different values of the number of cluster K. Fig. 9 presents the results obtained with $K = 2$ (Fig.9(a)), $K = 3$ (Fig.9(b)) and $K = 4$ (Fig.9(c)). When $K = 2$, the two regions of non-specific brain and the background outside the brain were merged, compared to the segmentation with $K = 3$. The striatum region which exhibited specific uptake was similar to the one obtained with $K = 3$. When $K = 4$, the striatum was split into two regions. Considering the shapes of the two regions, the splitting seemed to occur because of PVE causing local variation of the kinetic profiles near the non-specific brain region.

V. DISCUSSION

We have proposed an automatic and deterministic extension of the KSC approach for segmentation of dynamic PET images. First, a global optimization scheme for the cluster centroid identification was applied as the last step of the method to obtain deterministic results. Second, an unsupervised criterion called NMD was tailored and a stochastic global optimization

TABLE V
AVERAGE AND STANDARD DEVIATION FOR PFOM, ARI, NMD AND $\hat{\sigma}$ FOR 20 RUNS OF THE AD-KSC ALGORITHM ON 2 SLICES FROM SIMULATIONS 1,2 AND 3.

	PFOM	ARI	NMD	$\hat{\sigma}$
Axial Sim.1	0.92 ± 0.0039	0.90 ± 0.0035	0.83 ± 0.0099	0.08 ± 0.0112
Sagital Sim.1	0.99 ± 0.0004	0.91 ± 0.0019	0.90 ± 0.0133	1.93 ± 0.8017
Axial Sim.2	0.93 ± 0.0042	0.86 ± 0.0036	0.40 ± 0.0046	0.42 ± 0.1028
Sagital Sim.2	0.97 ± 0.0008	0.82 ± 0.0023	0.27 ± 0.0023	0.40 ± 0.0733
Axial Sim.3	0.92 ± 0.0047	0.68 ± 0.0042	0.20 ± 0.0039	1.03 ± 0.0767
Sagital Sim.3	0.69 ± 0.0009	0.83 ± 0.0048	0.13 ± 0.0041	0.68 ± 0.0674

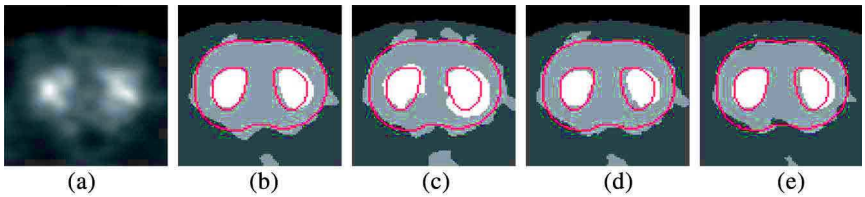

Fig. 7. Superimposition of the atlas edges with the results of KM, EM, HC, and AD-KSC applied on a dynamic PET image of a rat with $[^{18}F]LBT999$. (a) One frame from the dynamic sequence, (b) KM result, (c) EM result, (d) HC result, (e) AD-KSC result.

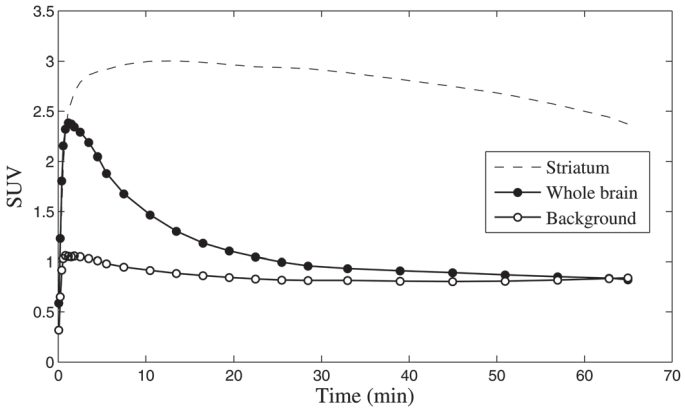

Fig. 8. TAC of the regions segmented by AD-KSC in $[^{18}F]LBT999$ PET image.

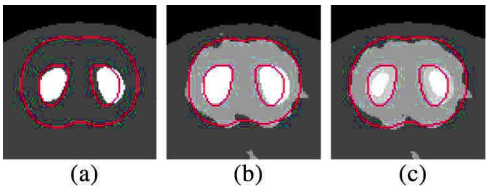

Fig. 9. Superimposition of the atlas edges with the results of AD-KSC applied on the dynamic PET image of the rat for different values of K. (a) AD-KSC with K = 2, (b) AD-KSC with K = 3 as presented in Fig. 7(e) (c) AD-KSC with K = 4.

method was used to automatically estimate the scale parameter of the method and the weight associated to each frame of the dynamic PET sequence. Our method is able to separate physiological clusters by mapping the kinetics of voxels into a high dimensional space and then cluster the projected data in a low-dimensional space. The results obtained with AD-KSC compare closely with those obtained with optimal manual parameterization of KSC method [19]. AD-KSC was compared to three other methods from the literature already used in dynamic PET and resulted in improved identification of functional regions. This improvement can be explained by the ability of AD-KSC to separate arbitrary shaped clusters. It also indicates that the global search procedure used to derive the final partition of the data led to acceptable settings of the parameters. The results also confirmed the deterministic property of D-KSC, guaranteeing a better convergence of the SA algorithm to the global minimum.

The NMD criterion was compared to the DI criterion. DI appeared very sensitive to noise or outlier, which was expected as it calculates the intra and inter-cluster distances using individual pairs of points. In comparison, NMD is a more robust criterion that can be used in the absence of ground truth. In our experiments using the simulated 4D PET data, the ground truth was available and the NMD score of the ground truth ROIs could be calculated. We found that in 65% of the studied slices, the NMD of ground truth was higher than the NMD obtained with AD-KSC. In the remaining 35% slices, the optimization of NMD by AD-KSC led to higher NMD scores. Without noise, the NMD of the ground truth is expected to be the maximum NMD value, however in the presence of noise, AD-KSC can reach higher values because there is no spatial constraint and NMD is optimized using SA for the estimation of the parameters (Fig. 5).

The AD-KSC algorithm includes the calculation of a Laplacian matrix derived from the similarity measures. The choice of the Laplacian matrix that is used has some influence on the clustering results. We chose the normalized Laplacian random walk L_{rw}. The clusters embedded into the low dimensional space using L_{rw} are very compact and points are mapped close to their centroid, which facilitates their separation by an hyperplan.

In this work, the AD-KSC method was applied on 2D+t data to reduce the computational complexity of the problem of eigendecomposition of large matrix. Clustering of the entire volume would probably improve the correct identification of the clusters. For such 3D+t computation, advanced mathematical tools for eigendecomposition or strategies that reduce the size of data have to be implemented.

The automatic selection of AD-KSC parameters (scale parameter and weighting factors) was performed by SA optimization of the NMD criterion. The variability of the estimated parameters was studied by running the AD-KSC several times. The ARI, PFOM and NMD criteria were almost constant despite small variations in the scale parameter and the weighting

factors. This variability can be explained by the fact that there is an interval of parameter values in which the results of segmentation are similar. The size of the interval is directly related to the separation between clusters. When the data are well separated the interval increases and several values of sigma and weighting factors can lead to the same results.

In our studies, we observed that the automatic selection of weights did not dramatically increase the scores of the results compared to the KSC weighting scheme. We also observed (results not shown) that using an identical weight for each frame yielded results close to the one we obtained using the automatic weight estimation. While this agrees with the results found in the literature [33], the gain offered by the automatic selection of the weights for some of the studied $2\mathrm{D}+\mathrm{t}$ slices favors its use as we never observed a less accurate segmentation when the weights were automatically estimated. Discarding weight estimation or replacing it with the inverse of a noise variance estimation remains possible if computation time is an issue, as it would reduce the number of parameters optimized by simulating annealing.

In AD-KSC, the number of clusters is selected *a priori*, as it is for all clustering methods used for comparison. The automatic selection of the number of clusters is a difficult issue for all clustering algorithms. While some methods or criteria have been proposed and could potentially be used for spectral clustering [20], [28], this aspect was not studied in this work. For application of AD-KSC to real images, the user should select the number of clusters based on some *a priori* knowledge. For instance, both six and four classes have been considered for the clustering of PET images of neuroinflammation [2], [3]. This number can also be selected *a posteriori*, after an analysis of the results with different numbers of clusters, as an incorrect number of clusters will lead to either split or merged functional regions (Fig. 9).

The PET images suffer from poor spatial resolution and partial volume effect (PVE) and the voxel value can be a mixture of two of more different functional signals. Therefore the TAC of the voxels affected by PVE can differ significantly from their true TAC. Areas near functional boundaries can be interpreted as distinct regions by clustering algorithms. While this issue could be reduced by partial volume effect correction, we did not use any in this study. Other undesirable artefacts come from the physiological motions that can severely impact the results of segmentation. In this study we used brain images for which motion artefacts are less frequent, but when applicable, movement correction methods should be used.

Supervised methods have been proposed to identify voxels as a weighted linear combination of kinetic classes. These methods, which have been successfully applied for the quantification of neuroinflammation [3], [2], require the definition of kinetic classes. They are usually defined from coregistered MRI data. AD-KSC could be used in complement with such methods to reduce the errors induced by coregistration and to define the classes from kinetic data only.

VI. Conclusion

A deterministic global search procedure was applied, and an unsupervised criterion was tailored and optimized by simulated annealing to automatically estimate the input parameters of the spectral clustering method. The usefulness of the proposed criterion and the deterministic property of the method were evaluated using GATE Monte Carlo simulations of PET images and a real data set. The AD-KSC results were found very close to the best results obtained with manual selection of the parameters. In addition, AD-KSC was compared with three other approaches: KM, EM, and HC. AD-KSC quantitatively outperformed these methods and improved the identification of functional regions without *a priori* knowledge on the kinetic model. The ROI defined by AD-KSC and the level of automation achieved might have significant impact for quantification of dynamic PET images, especially when no region of reference can be delineated.

Acknowledgment

The authors would like to thank the CNRS in Lebanon and Lebanese University for supporting this work.

References

[1] R. B. Banati, "Visualising microglial activation in vivo," *Glia*, vol. 40, pp. 206–217, 2002.

[2] F. Turkheimer, P. Edison, N. Pavese, F. Roncaroli, A. Anderson, A. Hammers, A. Gerhard, R. Hinz, Y. Tai, and D. Brooks, "Reference and target region modeling of $[^{11}\mathrm{C}]-(\mathrm{R})-\mathrm{PK11195}$ brain studies," *J. Nucl. Med.*, vol. 48, pp. 158–167, 2007.

[3] M. Yaqub, B. van Berckel, A. Schuitemaker, R. Hinz, F. Turkheimer, G. Tomasi, A. Lammertsma, and R. Boellaard, "Optimization of supervised cluster analysis for extracting reference tissue input curves in $(\mathrm{R})-[^{11}\mathrm{C}]\mathrm{PK11195}$ brain PET studies," *J. Cereb. Blood Flow Metab.*, vol. 32, pp. 1600–1608, 2012.

[4] K.-P. Wong, D. Feng, S. Meikle, and J. Fulham, "Segmentation of dynamic PET images using cluster analysis," *IEEE Trans. Nucl. Sci.*, vol. 49, pp. 200–207, 2002.

[5] Y. Kimura, M. Senda, and N. M. Alpert, "Fast formation of statistically reliable FDG parametric images based on clustering and principal components," *Phys. Med. Biol.*, vol. 47, pp. 455–468, 2002.

[6] J. G. Brankov, N. P. Galatsanos, Y. Yang, and M. N. Wernick, "Segmentation of dynamic PET or fMRI images based on a similarity metric," *IEEE Trans. Nucl. Sci.*, vol. 50, no. 5, pp. 1410–1414, Oct. 2003.

[7] M. Margadán-Méndez, A. Juslin, S. V. Nesterov, K. Kalliokoski, J. Knuuti, and U. Ruotsalainen, "Ica based automatic segmentation of dynamic $\mathrm{H}_2^{15}\mathrm{O}$ cardiac PET images," *Trans. Info. Tech. Biomed.*, vol. 14, pp. 795–802, 2010.

[8] A. Saad, B. Smith, G. Hamarneh, and T. Möller, "Simultaneous segmentation, kinetic parameter estimation, and uncertainty visualization of dynamic pet images," *Med. Image Comput. Comput. Assist. Interv.*, vol. 10, pp. 726–33, 2007.

[9] H. Guo, R. Renault, K. Chen, and E. Reiman, "Clustering huge data sets for parametric PET imaging," *Biosystems*, vol. 71, pp. 81–92, 2003.

[10] X. Zheng, G. Tian, S.-C. Huang, and D. Feng, "A hybrid clustering method for ROI delineation in small animal dynamic PET images: Application to the automatic estimation of FDG input functions," *IEEE Trans. Inf. Technol. Biomed.*, vol. 15, pp. 195–205, 2011.

[11] B. J. Parker and D. D. Feng, "Graph-based mumford shah segmentation of dynamic PET with application to input function estimation," *IEEE Trans. Nucl. Sci.*, vol. 52, no. 1, pp. 79–89, Feb. 2005.

[12] J. Kim, W. Cai, D. Feng, and S. Eberl, "Segmentation of VOI from multidimensional dynamic PET images by integrating spatial and temporal features," *IEEE Trans. Inf. Technol. Biomed.*, vol. 10, pp. 637–646, 2006.

[13] J. L. Chen, S. R. Gunn, M. S. Nixon, and R. N. Gunn, "Markov random field models for segmentation of pet images," *LNCS Inf. Process. Med. Imag.*, vol. 2082, pp. 468–474, 2001.

[14] R. Maroy, R. Boisgard, C. Comtat, V. Frouin, P. Cathier, E. Duchesnay, F. Dolle, P. E. Nielsen, R. Trebossen, and B. Tavitian, "Segmentation of rodent whole-body dynamic PET images: An unsupervised method based on voxel dynamics," *IEEE Trans. Med. Imag.*, vol. 27, pp. 342–354, 2008.

[15] E. Krestyannikov, J. Tohka, and U. Ruotsalainen, "Segmentation of Dynamic Emission Tomography Data in Projection Space," in *Computer Vision Approaches to Medical Image Analysis*. Berlin, Germany: Springer, 2006.

[16] M. E. Kamasak, "Clustering dynamic PET images on the Gaussian distributed sinogram domain," *Comput. Methods Programs Biomed.*, vol. 93, pp. 217–227, 2009.

[17] M. E. Kamasak and B. Bayraktar, "Clustering dynamic PET images on the projection domain," *IEEE Trans. Nucl. Sci.*, vol. 54, no. 3, pp. 496–503, Jun. 2007.

[18] M. E. Kamasak, C. A. Bouman, E. D. Morris, and K. Sauer, "Direct reconstruction of kinetic parameter images from dynamic pet data," *IEEE Trans. Med. Imag.*, vol. 24, pp. 636–650, 2005.

[19] S. Mouysset, H. Zbib, S. Stute, J. Girault, J. Charara, J. Noailles, S. Chalon, I. Buvat, and C. Tauber, "Segmentation of dynamic PET images with kinetic spectral clustering," *Phys. Med. Biol.*, vol. 58, pp. 6931–6944, 2013 [Online]. Available: http://dx.doi.org/10.1088/0031-9155/58/19/6931

[20] U. Luxburg, "A tutorial on spectral clustering," *Stat. Comput.*, vol. 17, pp. 395–416, 2007.

[21] J. Cheng-Liao and J. Qi, "Segmentation of mouse dynamic PET images using a multiphase level set method," *Phys. Med. Biol.*, vol. 55, pp. 6549–6569, 2010.

[22] J. Shi and J. Malik, "Normalized cuts and image segmentation," *IEEE Trans. Pattern Anal. Mach. Intell.*, vol. 22, pp. 888–905, 2000.

[23] A. Likas, N. Vlassis, and J. J. Verbeek, "The global K-means clustering algorithm," *Pattern Recognit.*, vol. 36, pp. 451–461, 2003.

[24] M. Rezaee, B. Lelieveldt, and J. Reiber, "A new cluster validity index for the fuzzy c-means," *Pattern Recognit. Lett.*, vol. 19, pp. 237–246, 1998.

[25] N. Zahid, O. Abouelala, M. Limouri, and A. Essaid, "Unsupervised fuzzy clustering," *Pattern Recognit. Lett.*, vol. 20, pp. 123–129, 1999.

[26] M. Halkidi and M. Vazirgiannis, "Clustering validity assessment: Finding the optimal partitionning of a data set," in *Proc. IEEE Int. Conf. Data Mining*, 2001, pp. 187–194.

[27] D. Davies and D. W. Bouldin, "A cluster separation measure," *IEEE Trans. Pattern Anal. Mach. Intell.*, vol. 1, pp. 224–227, 1979.

[28] J. C. Dunn, "A fuzzy relative of the isodata process and its use in the detecting compact well-separated clusters," *J. Cybern.*, vol. 3, pp. 32–57, 1973.

[29] R. H. Huesman, "A new fast algorithm for evaluation of regions of interest and statistical uncertainty in computer tomography," *Phys. Med. Biol.*, vol. 29, pp. 543–552, 1984.

[30] I. Buvat, "A non-parametric bootstrap approach for analyzing the statistical properties of SPECT and PET images," *Phys. Med. Biol.*, vol. 28, pp. 81–89, 2002.

[31] M. Dahlbom, "Estimation of image noise in PET using the bootstrap method," *IEEE Trans. Nucl. Sci.*, vol. 49, no. 5, pp. 2062–2066, Oct. 2002.

[32] C. T. Mesina, R. Boellaard, G. Jongbloed, A. W. van der Vaart, and A. A. Lammertsma, "Experimental evaluation of iterative reconstruction versus filtered back projection for 3D [^{15}O] water PET activation studies using statistical parametric mapping analysis," *Neuroimage*, vol. 19, pp. 1170–1179, 2003.

[33] M. Yaqub, R. Boellaard, M. A. Kropholler, and A. A. Lammertsma, "Optimisation algorithms and weighting factors for analysis of dynamic PET studies," *Phys. Med. Biol.*, vol. 51, pp. 4217–4232, 2006.

[34] S. Kirkpatrick, C. D. Gelett, and M. Vecchi, "Optimisation by simulated annealing," *Science*, vol. 220, pp. 671–680, 1983.

[35] S. Jan *et al.*, "GATE: A simulation toolkit for PET and SPECT," *Phys. Med. Biol.*, vol. 49, pp. 4543–4561, 2004.

[36] S. Jan *et al.*, "Gate v6: A major enhancement of the GATE simulation platform enabling modelling of CT and radiotherapy," *Phys. Med. Biol.*, vol. 56, pp. 881–901, 2011.

[37] I. G. Zubal, C. R. Harrell, E. O. Smith, Z. Rattner, G. Gindi, and P. B. Hoffer, "Computerized three-dimentional segmented human anatomy," *Med. Phys.*, vol. 21, pp. 299–302, 1994.

[38] W. Pratt, *Digital Image Processing*. Hoboken, NJ, USA: Wiley, 1977.

[39] W. M. Rand, "Objective criteria for the evaluation of clustering method," *J. Amer. Statist. Assoc.*, vol. 66, pp. 846–850, 1971.

[40] J. Ashburner, J. Haslam, C. Taylor, V. Cunningham, and T. Jones, "A cluster analysis for the characterisation of dynamic PET data," in *Quantification of Brain Function Using PET*. San Diego, CA, USA: Academic Press, 1996, ch. 59, pp. 301–306.

[41] A. Varrone, V. Stepanov, R. Nakao, M. Toth, B. Gulyas, P. Emond, J. Deloye, J. Vercouillie, M. Stabin, C. Jonsson, D. Guilloteau, and C. Halldin, "Imaging of the striatal and extrastriatal dopamine transporter with 18f-lbt-999: Quantification, biodistribution, and radiation dosimetry in nonhuman primates," *J. Nucl. Med.*, vol. 52, pp. 1313–1321, 2011.

[42] W. Schiffer, M. Mirrione, A. Biegon, D. Alexoff, V. Patel, and S. Dewy, "Serial micropet measures of the metabolic reaction to a microdialysis probe implant," *J. Neurosci. Methods*, vol. 155, pp. 272–284, 2006.